

# Measurement of the $\eta \rightarrow \pi^+ \pi^- \pi^0$ Dalitz plot distribution

P. Adlarson,<sup>1</sup> W. Augustyniak,<sup>2</sup> W. Bardan,<sup>3</sup> M. Bashkanov,<sup>4,5</sup> F.S. Bergmann,<sup>6</sup> M. Berłowski,<sup>7</sup> H. Bhatt,<sup>8</sup> A. Bondar,<sup>9,10</sup> M. Büscher,<sup>11,12,\*</sup> H. Calén,<sup>1</sup> I. Ciepał,<sup>3</sup> H. Clement,<sup>4,5</sup> D. Coderre,<sup>11,12,13,†</sup> E. Czerwiński,<sup>3</sup> K. Demmich,<sup>6</sup> E. Doroshkevich,<sup>4,5</sup> R. Engels,<sup>11,12</sup> A. Erven,<sup>14,12</sup> W. Erven,<sup>14,12</sup> W. Eyrich,<sup>15</sup> P. Fedorets,<sup>11,12,16</sup> K. Föhl,<sup>17</sup> K. Fransson,<sup>1</sup> F. Goldenbaum,<sup>11,12</sup> P. Goslawski,<sup>6</sup> A. Goswami,<sup>11,12,18</sup> K. Grigoryev,<sup>11,12,19,‡</sup> C.-O. Gullström,<sup>1</sup> F. Hauenstein,<sup>15</sup> L. Heijkenskjöld,<sup>1</sup> V. Hejny,<sup>11,12</sup> M. Hodana,<sup>3</sup> B. Höistad,<sup>1</sup> N. Hüken,<sup>6</sup> A. Jany,<sup>3</sup> B.R. Jany,<sup>3</sup> L. Jarczyk,<sup>3</sup> T. Johansson,<sup>1</sup> B. Kamys,<sup>3</sup> G. Kemmerling,<sup>14,12</sup> F.A. Khan,<sup>11,12</sup> A. Khoukaz,<sup>6</sup> D.A. Kirillov,<sup>20</sup> S. Kistryn,<sup>3</sup> H. Kleines,<sup>14,12</sup> B. Klos,<sup>21</sup> W. Krzemień,<sup>3</sup> P. Kulesa,<sup>22</sup> A. Kupść,<sup>1,7</sup> A. Kuzmin,<sup>9,10</sup> K. Lalwani,<sup>8,§</sup> D. Lersch,<sup>11,12</sup> B. Lorentz,<sup>11,12</sup> A. Magiera,<sup>3</sup> R. Maier,<sup>11,12</sup> P. Marciniowski,<sup>1</sup> B. Mariański,<sup>2</sup> B.V. Martemyanov,<sup>16</sup> U.-G. Meißner,<sup>11,12,23,24,25</sup> M. Mikirtychiants,<sup>11,12,13,19</sup> H.-P. Morsch,<sup>2</sup> P. Moskal,<sup>3</sup> H. Ohm,<sup>11,12</sup> I. Ozerianska,<sup>3</sup> E. Perez del Rio,<sup>4,5</sup> N.M. Piskunov,<sup>20</sup> P. Podkopał,<sup>3</sup> D. Prasuhn,<sup>11,12</sup> A. Pricking,<sup>4,5</sup> D. Pszczel,<sup>1,7</sup> K. Pysz,<sup>22</sup> A. Pysznik,<sup>1,3</sup> C.F. Redmer,<sup>1,¶</sup> J. Ritman,<sup>11,12,13</sup> A. Roy,<sup>18</sup> Z. Rudy,<sup>3</sup> S. Sawant,<sup>8,11,12</sup> S. Schadmand,<sup>11,12</sup> T. Sefzick,<sup>11,12</sup> V. Serdyuk,<sup>11,12,26</sup> B. Shwartz,<sup>9,10</sup> R. Siudak,<sup>22</sup> T. Skorodko,<sup>4,5</sup> M. Skurzok,<sup>3</sup> J. Smyrski,<sup>3</sup> V. Sopov,<sup>16</sup> R. Stassen,<sup>11,12</sup> J. Stepaniak,<sup>7</sup> E. Stephan,<sup>21</sup> G. Sterzenbach,<sup>11,12</sup> H. Stockhorst,<sup>11,12</sup> H. Ströher,<sup>11,12</sup> A. Szczurek,<sup>22</sup> A. Täschner,<sup>6</sup> A. Trzciński,<sup>2</sup> R. Varma,<sup>8</sup> M. Wolke,<sup>1</sup> A. Wrońska,<sup>3</sup> P. Wüstner,<sup>14,12</sup> P. Wurm,<sup>11,12</sup> A. Yamamoto,<sup>27</sup> X. Yuan,<sup>28</sup> L. Yurev,<sup>26,\*\*</sup> J. Zabierowski,<sup>29</sup> C. Zheng,<sup>28</sup> M.J. Zieliński,<sup>3</sup> A. Zink,<sup>15</sup> J. Złomańczuk,<sup>1</sup> P. Żuprański,<sup>2</sup> and M. Żurek<sup>11,12</sup>

(WASA-at-COSY Collaboration)

<sup>1</sup>*Division of Nuclear Physics, Department of Physics and Astronomy, Uppsala University, Box 516, 75120 Uppsala, Sweden*

<sup>2</sup>*Department of Nuclear Physics, National Centre for Nuclear Research, ul. Hoza 69, 00-681, Warsaw, Poland*

<sup>3</sup>*Institute of Physics, Jagiellonian University, ul. Reymonta 4, 30-059 Kraków, Poland*

<sup>4</sup>*Physikalisches Institut, Eberhard-Karls-Universität Tübingen, Auf der Morgenstelle 14, 72076 Tübingen, Germany*

<sup>5</sup>*Kepler Center für Astro- und Teilchenphysik, Physikalisches Institut der Universität Tübingen, Auf der Morgenstelle 14, 72076 Tübingen, Germany*

<sup>6</sup>*Institut für Kernphysik, Westfälische Wilhelms-Universität Münster, Wilhelm-Klemm-Str. 9, 48149 Münster, Germany*

<sup>7</sup>*High Energy Physics Department, National Centre for Nuclear Research, ul. Hoza 69, 00-681, Warsaw, Poland*

<sup>8</sup>*Department of Physics, Indian Institute of Technology Bombay, Powai, Mumbai-400076, Maharashtra, India*

<sup>9</sup>*Budker Institute of Nuclear Physics of SB RAS, 11 akademika Lavrentieva prospect, Novosibirsk, 630090, Russia*

<sup>10</sup>*Novosibirsk State University, 2 Pirogova Str., Novosibirsk, 630090, Russia*

<sup>11</sup>*Institut für Kernphysik, Forschungszentrum Jülich, 52425 Jülich, Germany*

<sup>12</sup>*Jülich Center for Hadron Physics, Forschungszentrum Jülich, 52425 Jülich, Germany*

<sup>13</sup>*Institut für Experimentalphysik I, Ruhr-Universität Bochum, Universitätsstr. 150, 44780 Bochum, Germany*

<sup>14</sup>*Zentralinstitut für Engineering, Elektronik und Analytik, Forschungszentrum Jülich, 52425 Jülich, Germany*

<sup>15</sup>*Physikalisches Institut, Friedrich-Alexander-Universität Erlangen-Nürnberg, Erwin-Rommel-Str. 1, 91058 Erlangen, Germany*

<sup>16</sup>*Institute for Theoretical and Experimental Physics, State Scientific Center of the Russian Federation, Bolshaya Cheremushkinskaya 25, 117218 Moscow, Russia*

<sup>17</sup>*II. Physikalisches Institut, Justus-Liebig-Universität Gießen, Heinrich-Buff-Ring 16, 35392 Giessen, Germany*

<sup>18</sup>*Department of Physics, Indian Institute of Technology*

*Indore, Khandwa Road, Indore-452017, Madhya Pradesh, India*

<sup>19</sup>*High Energy Physics Division, Petersburg Nuclear Physics Institute,*

*Orlova Rosha 2, Gatchina, Leningrad district 188300, Russia*

<sup>20</sup>*Veksler and Baldin Laboratory of High Energies Physics, Joint*

*Institute for Nuclear Physics, Joliot-Curie 6, 141980 Dubna, Russia*

<sup>21</sup>*August Chelkowski Institute of Physics, University of Silesia, Uniwersytecka 4, 40-007, Katowice, Poland*

<sup>22</sup>*The Henryk Niewodniczański Institute of Nuclear Physics, Polish*

*Academy of Sciences, 152 Radzikowskiego St, 31-342 Kraków, Poland*

<sup>23</sup>*Institute for Advanced Simulation, Forschungszentrum Jülich, 52425 Jülich, Germany*

<sup>24</sup>*Helmholtz-Institut für Strahlen- und Kernphysik, Rheinische*

*Friedrich-Wilhelms-Universität Bonn, Nußallee 14-16, 53115 Bonn, Germany*

<sup>25</sup>*Bethe Center for Theoretical Physics, Rheinische Friedrich-Wilhelms-Universität Bonn, 53115 Bonn, Germany*

<sup>26</sup>*Dzhelepov Laboratory of Nuclear Problems, Joint Institute*

*for Nuclear Physics, Joliot-Curie 6, 141980 Dubna, Russia*

<sup>27</sup>*High Energy Accelerator Research Organisation KEK, Tsukuba, Ibaraki 305-0801, Japan*  
<sup>28</sup>*Institute of Modern Physics, Chinese Academy of Sciences, 509 Nanchang Rd., Lanzhou 730000, China*  
<sup>29</sup>*Department of Cosmic Ray Physics, National Centre for  
Nuclear Research, ul. Uniwersytecka 5, 90-950 Łódź, Poland*  
(Dated: June 11, 2014)

Dalitz plot distribution of the  $\eta \rightarrow \pi^+ \pi^- \pi^0$  decay is determined using a data sample of  $1.2 \cdot 10^7$   $\eta$  mesons from  $pd \rightarrow {}^3\text{He} \eta$  reaction at 1 GeV collected by the WASA detector at COSY.

PACS numbers: 13.20.-v, 14.40.Aq

Keywords:  $\eta$  meson decays

---

\* present address: Peter Grünberg Institut, PGI-6 Elektronische Eigenschaften, Forschungszentrum Jülich, 52425 Jülich, Germany; Institut für Laser- und Plasmaphysik, Heinrich-Heine Universität Düsseldorf, Universitätsstr. 1, 40225 Dsseldorf, Germany

† present address: Albert Einstein Center for Fundamental Physics, University of Bern, Sidlerstrasse 5, 3012 Bern, Switzerland

‡ present address: III. Physikalisches Institut B, Physikzentrum, RWTH Aachen, 52056 Aachen, Germany

§ present address: Department of Physics and Astrophysics, University of Delhi, Delhi-110007, India

¶ present address: Institut für Kernphysik, Johannes Gutenberg-Universität Mainz, Johann-Joachim-Becher Weg 45, 55128 Mainz, Germany

\*\* present address: Department of Physics and Astronomy, University of Sheffield, Hounsfield Road, Sheffield, S3 7RH, United Kingdom

<i>Calculations:</i>	<i>Q</i>
LO [10]	15.6
NLO [10]	20.1
NNLO [10]	22.9
dispersive [13]	22.7(8)
dispersive [14]	22.4(9)
dispersive (PLM) [15]	23.1(7)
Lattice QCD av. [16]	22.6(7)(6)

TABLE I. Values of  $Q$  obtained from the  $\eta \rightarrow 3\pi$  decay. In addition a lattice QCD estimate is shown for comparison.

## I. INTRODUCTION

The amplitude of the isospin violating decays  $\eta \rightarrow \pi^+\pi^-\pi^0$  and  $\eta \rightarrow \pi^0\pi^0\pi^0$  is dominated by a term proportional to the light quark mass difference ( $m_d - m_u$ ) since the electromagnetic contribution is suppressed [1–3]. This makes the decays a sensitive probe of the light quark masses [4]. The leading term for the partial decay widths of the two decay modes is proportional to  $Q^{-4}$  where  $Q^2$  is defined as the following combination of the light quark masses [5]:

$$Q^2 = \frac{m_s^2 - \hat{m}^2}{m_d^2 - m_u^2}, \quad \hat{m} = \frac{1}{2}(m_u + m_d). \quad (1)$$

The determination of the  $Q$  parameter requires knowledge of the experimental value of at least one of the  $\eta \rightarrow \pi^+\pi^-\pi^0$ ,  $\eta \rightarrow \pi^0\pi^0\pi^0$  partial decay widths and the corresponding proportionality factors.

Experimental determination of the partial decay widths requires knowledge of the  $\eta$  radiative width,  $\Gamma_{\gamma\gamma}$ , and the relative branching ratios  $BR(\eta \rightarrow \pi^0\pi^0\pi^0)/BR(\eta \rightarrow \gamma\gamma)$  and  $BR(\eta \rightarrow \pi^+\pi^-\pi^0)/BR(\eta \rightarrow \gamma\gamma)$ . The radiative width could be determined by measuring cross section of the  $\eta$  meson two photon production using *e.g.* Primakov effect or  $e^\pm e^- \rightarrow e^\pm e^- \eta$  process. The knowledge of the Dalitz plot distributions for the  $\eta \rightarrow 3\pi$  decays will in principle contribute to all measurements involving these final states. For example  $\Gamma_{\gamma\gamma}$  was recently extracted from the cross section of the two photon production  $e^+e^- \rightarrow e^+e^- \eta$  where the  $\eta$  meson was tagged by the  $\eta \rightarrow \pi^0\pi^0\pi^0$  and  $\eta \rightarrow \pi^+\pi^-\pi^0$  decay modes [6].

The calculations of the proportionality factors could be carried out in the low energy effective field theory of the strong interactions, Chiral Perturbation Theory (ChPT). The process was calculated up to next-to-next-leading order (NNLO) [7–10]. The ChPT leading order (LO) result together with the measured value of the  $\eta \rightarrow \pi^+\pi^-\pi^0$  decay width of  $300 \pm 12$  eV [11] leads to  $Q$  equal 15.6 (Tab. I). The next-to-leading order (NLO) gives the  $Q$  value 28% larger where half of the increase comes from  $\pi\pi$  re-scattering between final state pions [9, 12]. Finally the NNLO order increases the value by an additional 14%. The values of  $Q$  extracted from various analyses are summarized in Tab. I.

The reliability of the calculations leading to the proportionality factor could be tested by comparing the experimental and theoretical Dalitz plots for both the neutral and charged modes. Such comparison constitutes a sensitive test of the convergence of the SU(3) ChPT expansion. For the neutral decay mode, where the Dalitz plot density is described by a single parameter up to quadratic terms, the experiments provide a consistent, precise value [17–25]. However, reproduction of this value has turned out to be a challenge for the ChPT calculations. For the  $\eta \rightarrow \pi^+\pi^-\pi^0$  decay mode, where there are more parameters to describe Dalitz plot density, there is basically only one modern, high statistics experiment [26].

The amplitudes for the  $\eta \rightarrow 3\pi$  decays could be also determined using unitarity and analyticity and the  $\pi\pi$  phase shifts up to some subtraction constants. These subtraction constants can be determined by matching to the results of the ChPT calculations [13, 14] and thus improving convergence of the ChPT expansion. Alternatively the subtraction constants can be obtained directly from fits to the experimental Dalitz plot distributions using only the most reliable constraints from ChPT. In recent years two such data driven dispersive approaches have emerged: from Bern-Lund-Valencia (BLV) group [27] and from Prague-Lund-Marseille (PLM) group [15]. Both approaches rely in large extent on the experimental Dalitz plot data from and promise a precise determination of  $Q$ .

Another aspects of the  $\eta \rightarrow 3\pi$  decay such as isospin violation effects in low-energy  $\pi\pi$  scattering are addressed by Non-Relativistic Effective Field Theory (NREFT), developed first for low-energy  $\pi\pi$  scattering

<i>Calculations</i>	<i>-a</i>	<i>b</i>	<i>d</i>	<i>f</i>	<i>g</i>
LO [10]	1.039	0.27	0.000	0.000	—
NLO [10]	1.371	0.452	0.053	0.027	—
NNLO [10]	1.271(75)	0.394(102)	0.055(57)	0.025(160)	—
dispersive [14]	1.16	0.26	0.10	—	—
tree disp [32]	1.10	0.31	0.001	—	—
abs disp [32]	1.21	0.33	0.04	—	—
NREFT [30]	1.213(14)	0.308(23)	0.050(3)	0.083(19)	-0.039(2)
BSE [31]	1.054(25)	0.185(15)	0.079(26)	0.064(12)	—
<i>Experiment</i>	<i>-a</i>	<i>b</i>	<i>d</i>	<i>f</i>	<i>g</i>
Gormley [33]	1.17(2)	0.21(3)	0.06(4)	—	—
Layter <i>et al</i> [34]	1.080(14)	0.03(3)	0.05(3)	—	—
CBarrel-98 [35]	1.22(7)	0.22(11)	0.06 (fixed)	—	—
KLOE [26]	1.090(5) <sub>(-8)</sub> <sup>(+19)</sup>	0.124(6)(10)	0.057(6) <sub>(-16)</sub> <sup>(+7)</sup>	0.14(1)(2)	~ 0

TABLE II. Dalitz plot parameters from theoretical predictions and experimental results for  $\eta \rightarrow \pi^+\pi^-\pi^0$ . Results at LO, NLO and NNLO ChPT are taken from [10]. The values inside the parentheses denote the quoted uncertainties. For the KLOE data both statistical and systematic uncertainties are given.

and decay  $K \rightarrow 3\pi$  [28] decays and subsequently was applied to  $\eta \rightarrow 3\pi$  decays [29, 30]. A more model dependent analysis providing uniform treatment of all three pseudoscalar  $\eta$  and  $\eta'$  decay modes, including  $\eta \rightarrow 3\pi$  was pursued in Ref. [31].

The Dalitz plot for  $\eta \rightarrow \pi^+\pi^-\pi^0$  is expressed using normalized variables  $X$  and  $Y$ :

$$X = \sqrt{3} \frac{T_+ - T_-}{Q_\eta}; \quad Y = \frac{3T_0}{Q_\eta} - 1, \quad (2)$$

where  $T_+$ ,  $T_-$ ,  $T_0$  are kinetic energies of the charged and neutral pions in the  $\eta$  meson rest frame.  $Q_\eta$  is the excess energy for the decay:

$$Q_\eta = T_+ + T_- + T_0 \quad (3)$$

or equivalently  $Q_\eta = m_\eta - 2m_\pm - m_0$  where  $m_\pm$  and  $m_0$  are the masses of the charged and neutral pions. A polynomial parametrization is often used to represent the squared amplitude for the decay:

$$|\mathcal{A}(X, Y)|^2 \propto \rho(X, Y) = N (1 + aY + bY^2 + cX + dX^2 + eXY + fY^3 + gX^2Y + hX^3), \quad (4)$$

where  $\rho(X, Y)$  is the Dalitz plot density,  $N$  is a normalization factor and  $a, b, \dots, g, h$  are *Dalitz plot parameters*. The terms with odd powers of the  $X$  variable, like  $c$ ,  $e$  and  $h$ , should be zero as they imply charge conjugation violation in strong or electromagnetic interactions. The Dalitz plot parameters from various theoretical predictions and from experiments are given in Tab. II.

The best precision in the experimental Dalitz plot parameter values is achieved in the recent KLOE [26] experiment from the analysis of  $1.34 \cdot 10^6$   $\eta \rightarrow \pi^+\pi^-\pi^0$  decays. The description of the KLOE data requires inclusion of a cubic term (the  $f$  parameter). The quadratic term  $b$  disagrees with the experimental results from the seventies [33, 34], while it agrees with the Crystal Barrel results [35] within uncertainties. A comparison of the KLOE result to the theoretical predictions shows disagreement for both the  $a$  and  $b$  parameter values when taking into account the combined uncertainties of the experimental and theoretical predictions. The discrepancies are more than five standard deviations for the NNLO parameter  $a$  and  $b$  values. Also, model independent relations between neutral and charged Dalitz plot parameters show tensions [30].

A solid experimental data base for the Dalitz plot distributions is a must for the further more detailed investigations. The next goal is to reach a comparable experimental status for the charged  $\eta \rightarrow \pi^+\pi^-\pi^0$  channel as for the neutral  $\eta \rightarrow \pi^0\pi^0\pi^0$ . Therefore, several new high statistics measurements of the charged channel are required.

Here we present a first step to match the KLOE precision with an independent measurement of the  $\eta \rightarrow \pi^+\pi^-\pi^0$  Dalitz plot parameters.

## II. EXPERIMENT

### A. The WASA detector

The presented results are obtained with the WASA detector [36, 37], in an internal target experiment at the Cooler Synchrotron COSY storage ring [38], Forschungszentrum Jülich, Germany. The COSY proton beam interacts with an internal target consisting of small pellets of frozen deuterium (diameter  $\sim 35 \mu\text{m}$ ). The  $\eta$  mesons for the  $\eta \rightarrow 3\pi$  decay studies were produced using the  $pd \rightarrow {}^3\text{He}\eta$  reaction at a proton kinetic energy of 1 GeV, corresponding to a center-of-mass excess energy of 60 MeV. The cross section of the reaction is  $0.40(3) \mu\text{b}$  at this energy [39, 40].

The WASA detector consists of a Central Detector (CD) and a Forward Detector (FD), covering scattering angles of  $20^\circ$ – $169^\circ$  and  $3^\circ$ – $18^\circ$  respectively in combination with an almost full azimuthal angle coverage. The Central Detector is used to detect and measure the decay products of the mesons. A straw cylindrical chamber (MDC) is placed in a magnetic field, provided by a superconducting solenoid, for momentum determination of charged particles. The central value of the magnetic field was 0.85 T during the experiment. The electromagnetic calorimeter consists of 1012 CsI(Na) crystals read-out by photomultipliers. A plastic scintillator barrel is placed between the MDC and the solenoid allowing particle identification and accurate timing for charged tracks. The Forward Detector consists of thirteen layers of plastic scintillators providing energy and time information and a straw tube tracker for precise track reconstruction.

At the trigger level events with at least one track in the forward detector and with a high energy deposit in thin plastic scintillator layers were accepted. The condition is effective for selection of  ${}^3\text{He}$  ions and provides an unbiased data sample of  $\eta$  meson decays. The proton beam energy was chosen so the  ${}^3\text{He}$  produced in the  $pd \rightarrow {}^3\text{He}\eta$  reaction stop in the first thick scintillator layer of the Forward Detector.

The correlation plot  $\Delta E - \Delta E$  from a thin layer and the first thick layer of the FD is shown in Fig. 1(left). The (upper) band corresponding to the  ${}^3\text{He}$  ion is well separated from the bands for other particles and allows a clear identification of  ${}^3\text{He}$ . The  ${}^3\text{He}$  from the reaction of interest has kinetic energies ranging between 220 MeV and 460 MeV and scattering angles ranging from  $0^\circ$  to  $10^\circ$ .

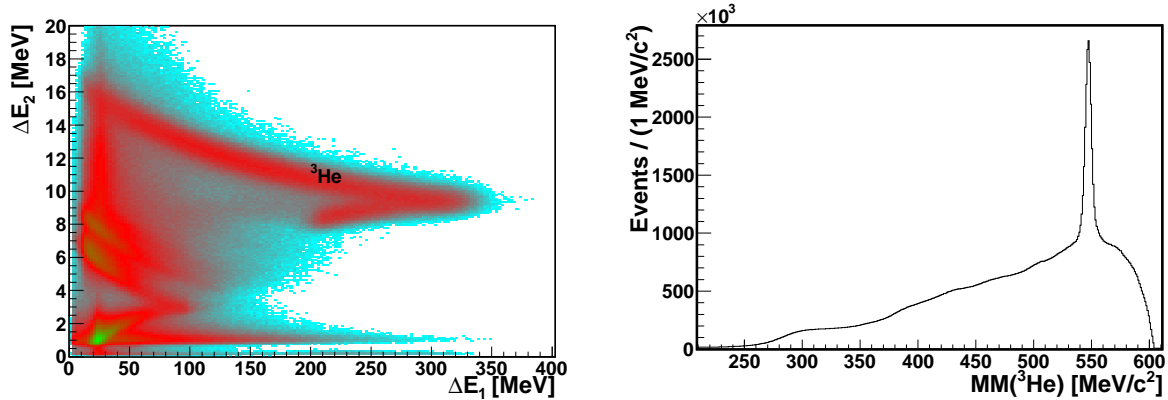


FIG. 1. (left) Correlation of energy deposits between two Forward Detector plastic detector layers: the first thick layer (11 cm),  $\Delta E_1$ , and a preceding thin (0.5 cm) layer,  $\Delta E_2$ . (right)  $MM({}^3\text{He})$  for all events with a  ${}^3\text{He}$  detected in the FD. There are about  $1.2 \cdot 10^7$  events in the peak corresponding to the  $pd \rightarrow {}^3\text{He}\eta$  reaction.

The missing mass calculated from the reconstructed  ${}^3\text{He}$  momentum,  $MM({}^3\text{He})$ , is shown in Fig. 1(right). The  $\eta$  peak has a width of  $6.2 \text{ MeV}/c^2$  (FWHM) and contains about  $1.2 \cdot 10^7$  events. The luminosity during the run was kept in range  $(1 - 5) \times 10^{31} \text{ cm}^{-2}\text{s}^{-1}$ .

### B. Simulation

The measurement of the production reaction  $pd \rightarrow {}^3\text{He}\eta$  is simulated by using the experimental angular distribution from [39, 40]. The decay  $\eta \rightarrow \pi^+\pi^-\pi^0$  ( $\text{BR}=22.92(28)\%$  [11]) was simulated at the final stage using the central values of the extracted experimental Dalitz plot parameters. The main physics background

processes include the  $\eta \rightarrow \pi^+\pi^-\gamma$  (BR=4.22(8)% [11]) decay and the direct two and three pion production reactions:  $pd \rightarrow {}^3\text{He}\pi^+\pi^-$ ,  $pd \rightarrow {}^3\text{He}\pi^+\pi^-\pi^0$ . For the  $\eta \rightarrow \pi^+\pi^-\gamma$  we used the results reported in [41, 42]. All other  $\eta$  decay channels contribute marginally to the final result and may therefore be neglected. The direct  $3\pi$  production channel simulated with uniform phase space distributions were modified to reproduce our final MM( ${}^3\text{He}$ ) distribution as extracted from Fig. 3.

The chance coincidental events for the 16 most prominent  $pd$  reaction channels (total cross section 80 mb) and the effect of energy pile-up in the different detector elements are also included in the simulation. Their relative strengths of the different channels are assumed using the Fermi statistical model. For the quasi-free break up reactions the relative momentum between the np-pair is simulated using the deuteron wave function is used while for all other channels uniform phase space is assumed.

The accelerator and the target pellet beam overlap region is 3.8 mm in the horizontal and 5 mm in the vertical direction. The interaction point distribution can have tails in the  $z$ -direction since the accelerator beam can also interact with a small fraction of the surrounding rest gas or divergent pellets. The shape of the tails is based on the  $z$ -vertex distribution deduced from experimental data with  ${}^3\text{He}$  production.

### C. Event selection

The signature of an event, in addition to the  ${}^3\text{He}$  ion reconstructed in FD, is at least two tracks from charged particles in the MDC and at least two clusters in the calorimeter not associated with the tracks. The polar angles of charged particles detected in the MDC are larger than  $30^\circ$  and less than  $150^\circ$ . The time window in the CD with respect to the time signal of the  ${}^3\text{He}$  is 6.2 ns for the charged particle tracks and 30 ns for neutral particle hit. All possible combinations of tracks are retained for kinematic fitting even if the number of tracks in the event is greater than the expected number of final state particles.

The point of closest approach of the two charged particle tracks of the CD should be within 7 cm from the center of the pellet and COSY beams overlap region. A kinematic fit with the

$$pd \rightarrow {}^3\text{He}\pi^+\pi^-\gamma\gamma \quad (5)$$

reaction hypothesis is applied and the combination with the lowest  $\chi^2$  value is selected. A cut on the  $\chi^2$  probability is made at 1%. In the remaining analysis the variable values adjusted by the fit are used. The correlation between the fitted MM( ${}^3\text{He}$ ) and the invariant mass of the two photons, IM( $\gamma\gamma$ ), is shown in Fig. 2(left).

Fig. 2(right) shows the extracted yield of the  $pd \rightarrow {}^3\text{He}\eta$  events as a function of IM( $\gamma\gamma$ ). The distribution was obtained by creating 2 MeV/ $c^2$  horizontal slices of the scatter plot in Fig. 2(left) and determining the peak content of each one. The resulting distribution agrees well with simulations of the  $\eta \rightarrow \pi^+\pi^-\pi^0$  and  $\eta \rightarrow \pi^+\pi^-\gamma$  decays. The relative normalization between the two decays is fixed by their branching ratios. For the final data sample only events with IM( $\gamma\gamma$ ) > 100 MeV/ $c^2$  are selected.

The data sample used in this analysis consists of  $1.74 \cdot 10^5$   $\eta$  candidates. The comparison of the simulated and experimental distributions of MM( ${}^3\text{He}$ ) is shown in Fig. 3. The dominating background comes from direct three pion production. The contributions from two pion production and the  $\eta \rightarrow \pi^+\pi^-\gamma$  decay are less than 1%.

## III. RESULTS

The variables  $X$  and  $Y$  are calculated from Eqn. (2) using the kinetic energies of the charged pions after the kinematic fitting boosted to the rest frame of the  $\pi^+\pi^-\gamma\gamma$  system. For the variables after the kinematic fit of the reaction (5) one has  $\mu \equiv \text{IM}(\pi^+\pi^-\gamma\gamma) = \text{MM}({}^3\text{He})$ . However,  $\mu$  is not constrained to equal  $m_\eta$  and IM( $\gamma\gamma$ ) not constrained to  $m_0$ . Therefore, the kinetic energy of the neutral pion,  $T_0$ , is determined in the following way:

$$T_0 = \mu - T_+ - T_- - 2m_\pm - \text{IM}(\gamma\gamma), \quad (6)$$

and for calculating  $Q_\eta$  we use Eqn. (3).

The selected Dalitz plot bin width in  $X$  and  $Y$  ( $\Delta X = \Delta Y = 0.2$ ) is in our case limited by the statistics needed for background subtraction and reliable systematical crosschecks. The uncertainty of the  $X$  and  $Y$



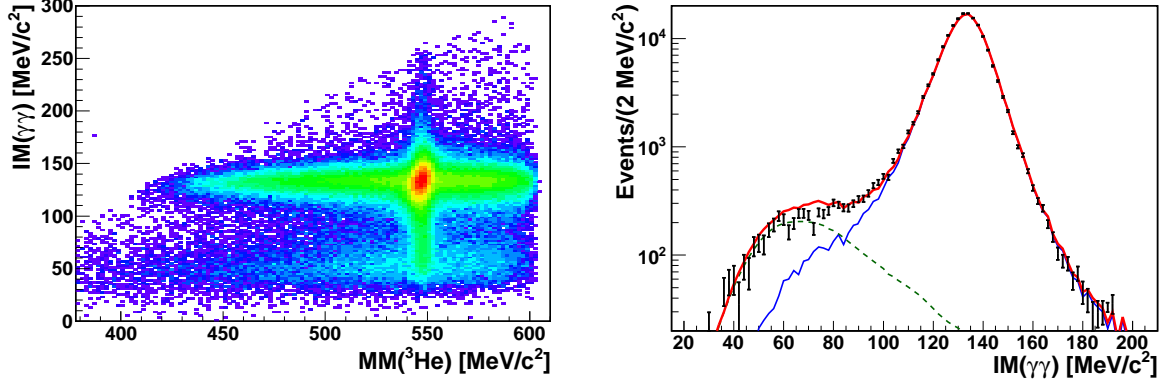


FIG. 2. (left) Correlation between  $MM(^3\text{He})$  and  $IM(\gamma\gamma)$  for variables adjusted by a kinematic fit. (right) Comparison of the experimental and simulated contributions of the  $\eta$  events as the function of  $IM(\gamma\gamma)$ . The extracted number of the events in the  $\eta$  peak for each  $2 \text{ MeV}/c^2$   $IM(\gamma\gamma)$  slice is well described by the simulation (thick solid red line) including the  $\eta \rightarrow \pi^+\pi^-\pi^0$  (solid blue line) and  $\eta \rightarrow \pi^+\pi^-\gamma$  decays (dashed green line).

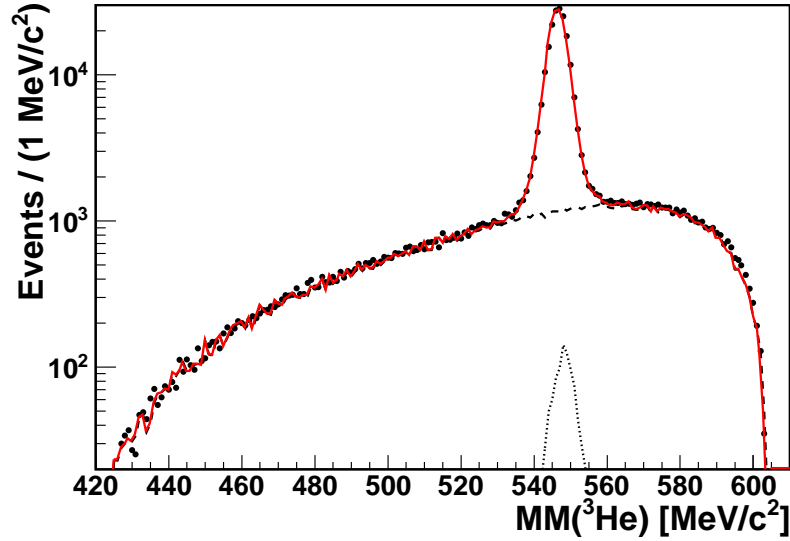


FIG. 3. The distribution of  $MM(^3\text{He})$  using variables adjusted by the kinematic fit for the final data sample (dots), agree well with the sum of the Monte Carlo distributions for the signal and the backgrounds (red solid line). Separately are shown contributions from  $\eta \rightarrow \pi^+\pi^-\gamma$  (dotted line) and from the direct  $3\pi$  production (dashed line).

measurement is well within the experimental resolution (FWHM of approximately 0.10 for both  $\Delta X$  and  $\Delta Y$  in average). The  $X, Y$  region  $[-1.1, 1.1] \times [-1.1, 1.1]$  is divided into  $11 \times 11$  bins. The border bins with less than 90% Dalitz plot area inside the kinematic boundaries are excluded leading to 59 bins used in the analysis. Definition and the numbering scheme of the bins is given in Fig. 4.

The Dalitz plot for the  $\eta \rightarrow \pi^+\pi^-\pi^0$  decay is obtained by dividing the reconstructed  $X$  and  $Y$  variables into bins and determining the signal content in each bin from the corresponding  $\mu$  distribution. The signal content in each bin is estimated by a least squared fit of the simulated data of  $pd \rightarrow ^3\text{He}\eta$  and the  $pd \rightarrow ^3\text{He}\pi^+\pi^-\pi^0$  continuum background reaction. The matrix element squared of the background reaction is assumed to be a linear function of  $\mu$ :

$$F_i(\mu) = N_S^i s_i(\mu) + N_B^i (1 + \alpha_i \mu) b_i(\mu), \quad (7)$$

where  $i$  is the Dalitz plot bin number,  $N_S^i$  is the normalization factor for the simulated  $pd \rightarrow ^3\text{He}\eta$  signal,

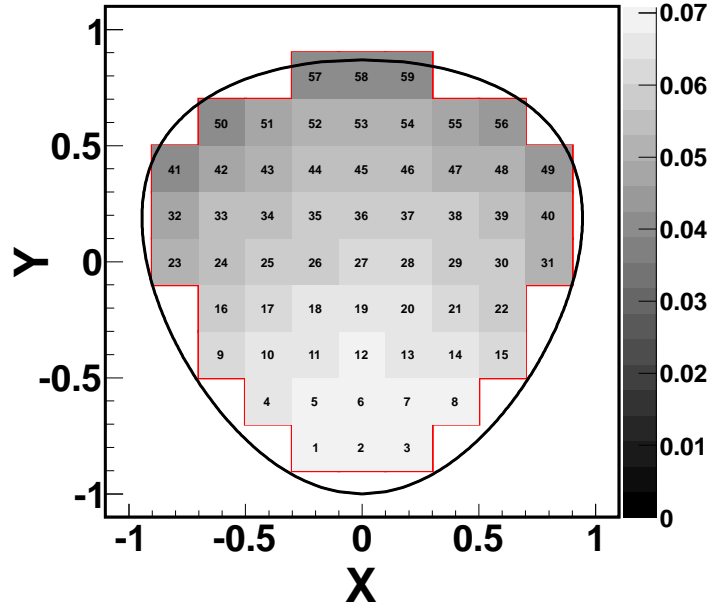


FIG. 4. Position and numbering of the Dalitz plot bins used for the analysis. The acceptance for the  $\eta \rightarrow \pi^+\pi^-\pi^0$  decay is also indicated by the gray scale.

$s_i(\mu)$ .  $N_B^i, b_i(\mu)$  have the corresponding meaning with respect to the flat phase space simulation of the  $pd \rightarrow {}^3\text{He}\pi^+\pi^-\pi^0$  reaction.  $N_S^i, N_B^i$  and  $\alpha_i$  are free parameters in the fit.

Two examples of the fits are shown in Fig. 5; one for a Dalitz plot bin with larger statistics (bin #2, centered at  $X = 0, Y = -0.8$ ) and one for a bin with lower statistics, (bin #53, centered at  $X = 0, Y = 0.6$ ).

Finally the simulated background from  $\eta \rightarrow \pi^+\pi^-\gamma$  events is subtracted from  $N_S^i$ . This contribution is small compared to the statistical uncertainties. The extracted number of  $\eta \rightarrow 3\pi$  events is corrected for acceptance. It was checked that the use of bin by bin acceptance correction (*i.e.* diagonal smearing matrix) does not introduce any significant systematic effect.

The acceptance values, indicated in Fig. 4, are obtained from a MC sample of  $5 \cdot 10^7$   $\eta \rightarrow \pi^+\pi^-\pi^0$  events and varies between 4% and 7%. It is larger when  $T_0$  is small (*i.e.* lower  $Y$ -values), but also when the kinetic energies of the two charged pions are similar (*i.e.* for  $X$  close to zero). Fig. 6 shows the acceptance corrected number of  $\eta \rightarrow \pi^+\pi^-\pi^0$  events as function of the Dalitz plot bin number.

The Dalitz plot parameters are obtained with the least square fitting procedure which minimizes

$$\chi^2 = \sum_{i=1}^{59} \left( \frac{N_i - \rho(X_i, Y_i)}{\Delta N_i} \right)^2. \quad (8)$$

$N_i$  and  $\Delta N_i$  denote the acceptance corrected number of events and their statistical uncertainty for the Dalitz plot bins  $i = 1, \dots, 59$ . The function  $\rho(X_i, Y_i)$ , defined in Eqn. (4), is evaluated at the center of each Dalitz plot bin:  $X_i$  and  $Y_i$ . In our case the systematic effects introduced by this procedure are negligible as it was checked using MC data sample. The overall normalization factor  $N$  is also a free parameter in the fit.

The obtained Dalitz plot parameters together with their statistical uncertainties are presented in Tab. III for different assumptions about the Dalitz plot parameters together with the fit  $\chi^2$  and number of degrees of freedom (*dof*). The  $c$  and  $e$  parameters are fixed to 0 in the fits. In addition we have performed fits including these parameters. The result gives  $c$  and  $e$  consistent with zero:  $c = -0.007(9)$  and  $e = -0.020(23)$  and does not affect other parameters. For the case when all  $a, b, c, d, e$  and  $f$  parameters are fit one obtains  $\chi^2/\text{dof} = 46.6/52$ . The correlation matrix between the fitted parameters for the standard result obtained is shown in Tab. IV.

Tab. IV shows a strong anti-correlation between the parameter  $a$  and  $f$  which is also reflected in the uncertainties of the parameter  $a$ . The bins of the Dalitz plot are compared in Fig. 6 to the parametrization



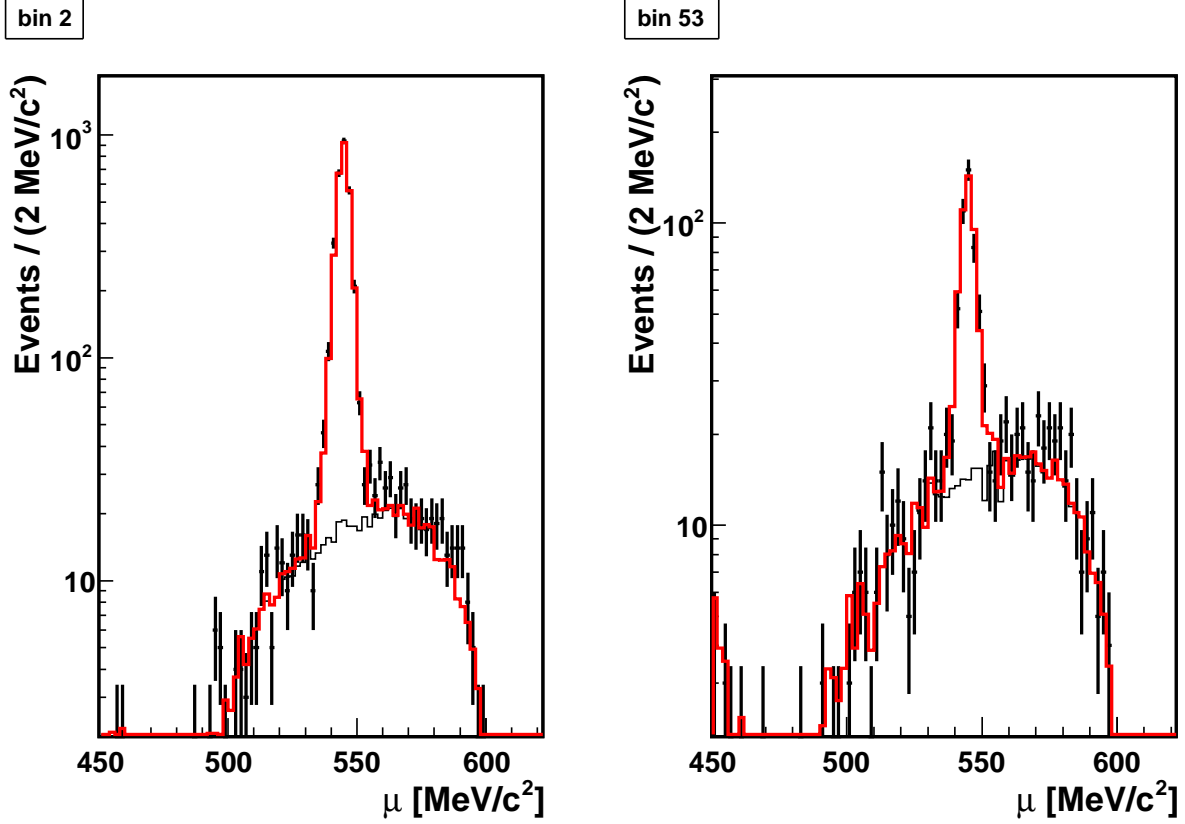


FIG. 5. Two examples of the fits to the  $dN/d\mu$  distributions for a large (left) and a low statistics Dalitz plot bin (right). The red thick line is the fitted function Eq. 7 while the thin line represents the continuous background contribution.

	$a$	$b$	$d$	$f$	$\chi^2/dof$
4 parameters ( <i>std</i> )	-1.144(18)	0.219(19)	0.086(18)	0.115(37)	49.4 / 54
3 parameters	-1.101(11)	0.234(19)	0.078(18)	0 (fix)	58.8 / 55
2 parameters	-1.075(9)	0.201(17)	0 (fix)	0 (fix)	78.3 / 56

TABLE III. Fit results for different sets of Dalitz plot parameters. The normalization factor,  $N$ , is omitted from the table. A number followed by '(fix)' means that the corresponding parameter was fixed to this number.

with four free parameters  $a, b, d, f$  where the remaining ones are set to zero (parametrization labeled as *std* in Tab. III).

#### IV. SYSTEMATIC UNCERTAINTIES

The systematic uncertainties of the obtained Dalitz plot parameters are investigated by including variations due to know sources of uncertainties in the MC generated data and by changing the selection criteria to find the remaining effects. In particular the consistency of extraction of the Dalitz plot distribution and fitting of the Dalitz plot parameters were tested using MC generated data ten times larger than in the experiment. The input parameters were reproduced without introducing any systematical deviation within the statistical uncertainties.

One of the most important sources of systematical uncertainties is the direct background subtraction procedure. This uncertainty is estimated by comparing a fit with the signal region excluded from the fit

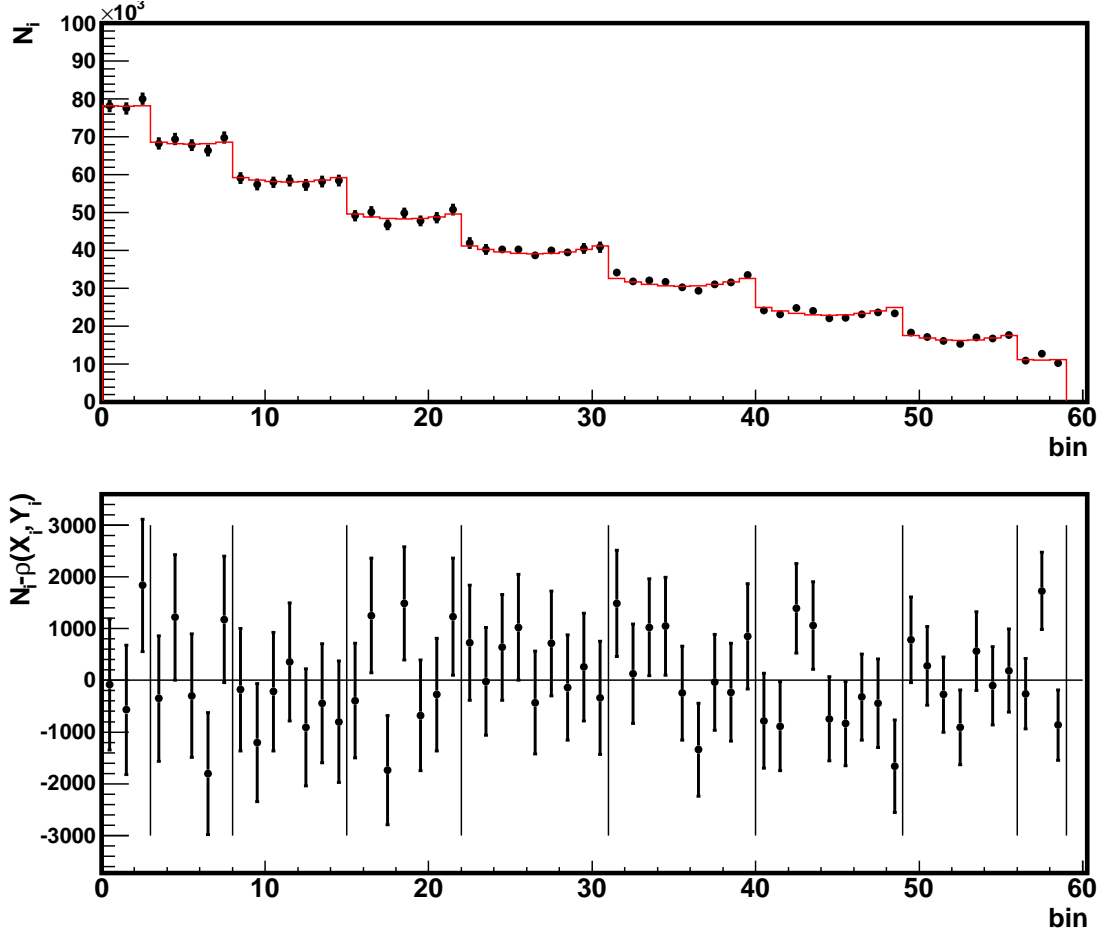


FIG. 6. The upper panel shows acceptance corrected Dalitz plot bin contents with statistical uncertainties (black points with error bars) compared to the fitted function  $\rho(X, Y)$  (red line) for each bin. The lower panel shows the corresponding residuals.

	$a$	$b$	$d$
$b$	-0.24		
$d$	-0.45	0.36	
$f$	-0.79	-0.25	0.14

TABLE IV. Correlation matrix for the Dalitz plot parameters.

and the signal term  $N_S^i s_i(\mu)$  in Eqn. (7) is omitted and the background is subtracted directly from the data ([Test 1] in Tab. V).

To investigate further possible systematical effects the data sample has been divided into sets of high and low luminosity. The  $pd \rightarrow X$  cross section is  $\sim 80$  mb, which amounts to few background reactions produced per  $\mu s$ . The largest effect is connected to the calorimeter signals since the decay times are of the order of  $\mu s$ . The Dalitz plot parameter values obtained for the low and high luminosity sample are shown by [Test 2] in Tab. V.

Two different accelerator beam modes were used during the beam time and they cover roughly equal time of data taking. In the first half, a constant beam energy during the accelerator cycle was assured by a fixed radio frequency (RF). In the second half, a coasting beam with RF switched off swept the target leading to a slight decrease of the beam energy during a cycle (from 1000.0 MeV to 993.5 MeV). In the experimental analysis this energy decrease is taken into account. However, in the simulations the acceptance has been

calculated for a beam kinetic energy fixed at 1 GeV. The comparison of the two cases ([Test 3] in Tab. V) shows the largest deviation for the  $b$  parameter ( $\approx 2\sigma$ ). To investigate the source of the effect we have calculated the acceptances also for the lowest beam energy in the RF off mode (993.5 MeV) and concluded that the change is too small to explain the observed deviation.

The effect of the uncertainty of the implemented detector resolution in the detector simulations is tested by increasing the kinematic fit probability from 0.01 to 0.1 ([Test 4] in Tab. V). The difference between the parameter values are not significant and are therefore neglected in the final systematical uncertainty.

	$-a$	$b$	$d$	$f$	$\chi^2 / d.o.f.$
Standard result	1.144(18)	0.219(19)	0.086(18)	0.115(37)	49.4 / 54
[Test 1] Background fit	1.126(18)	0.230(19)	0.094(18)	0.111(37)	60.5 / 54
[Test 2] Low luminosity	1.130(24)	0.216(26)	0.059(24)	0.104(50)	50.5 / 54
[Test 2] High luminosity	1.164(25)	0.219(28)	0.106(26)	0.152(52)	54.9 / 54
[Test 3] RF	1.127(26)	0.177(28)	0.085(27)	0.140(55)	56.1 / 54
[Test 3] No RF	1.139(23)	0.252(26)	0.076(24)	0.069(49)	49.6 / 54
[Test 4] PDF > 0.1	1.146(22)	0.224(24)	0.075(22)	0.117(46)	48.0 / 54

TABLE V. Dalitz plot parameters extracted for different tests for systematic effects. Description in the text.

The only significant changes are seen for the  $b$  parameter for the two accelerator operation modes and for  $d$  for the two luminosity cases. We use methodology of Ref. [43] and express the final result for the Dalitz plot parameters in the following way:

$$\begin{aligned}
-a &= 1.144 \pm 0.018(stat) \\
b &= 0.219 \pm 0.019(stat) \pm 0.037(syst) \\
d &= 0.086 \pm 0.018(stat) \pm 0.018(syst) \\
f &= 0.115 \pm 0.037(stat).
\end{aligned}$$

In addition we give the values for the C violating parameters  $c$  and  $e$ :

$$\begin{aligned}
c &= -0.007 \pm 0.009(stat) \\
e &= -0.020 \pm 0.023(stat) \pm 0.029(syst).
\end{aligned}$$

The results are dominated by statistical uncertainties and therefore the provided table with acceptance corrected bin contents, Tab. VI, could be used directly for comparison with theoretical models.

## V. DISCUSSION OF RESULTS

Parameters  $a$ ,  $b$  and  $d$  significantly deviate from zero. The  $d$  parameter is  $3.4\sigma$  above zero. From Tab. III it is seen that  $\chi^2$  per  $dof$  is only slightly worse if parameter  $f$  is set to zero in the fit. The significance of allowing  $f \neq 0$  in our data is  $3.1\sigma$ . However, the  $a$  and  $f$  parameters are strongly anti-correlated (see Tab. IV) and excluding  $f$  from the fit affects also the  $a$  value. The data do not require higher order terms in the polynomial expansion such as  $g \cdot X^2Y$  and  $h \cdot X^3$ .

Here we list deviations from the Dalitz plot parameters obtained by the KLOE collaboration [26] together with their significance (statistical and systematic uncertainties are added in squares):

$$\begin{aligned}
-\Delta a &= +0.054(23) \quad (+2.3\sigma) \\
\Delta b &= +0.095(44) \quad (+2.2\sigma) \\
\Delta d &= +0.029(28) \quad (+1.0\sigma) \\
\Delta f &= -0.025(43) \quad (-0.6\sigma).
\end{aligned}$$

Our results are generally consistent with KLOE, however there is some tension for  $a$  and  $b$  parameters. Our data confirm the discrepancies between theoretical calculations and the experimental values from the

KLOE experiment. The provided experimental data points of the individual Dalitz plot bins will allow independent analyses using NREFT or dispersive methods.

The presented results are based on a first part of the WASA-at-COSY data from the  $pd \rightarrow {}^3\text{He}\eta$  reaction. More data are available from WASA-at-COSY also from the  $pp \rightarrow pp\eta$  reaction. Together with expected results from other experiments the goal of a precise determination of the  $\eta \rightarrow \pi^+\pi^-\pi^0$  Dalitz plot parameters might soon be reached.

Bin #	Content	Bin#	Content	Bin #	Content	Bin #	Content
1	$2.020 \pm 0.033$	16	$1.271 \pm 0.029$	31	$1.058 \pm 0.028$	46	$0.573 \pm 0.021$
2	$2.004 \pm 0.032$	17	$1.296 \pm 0.029$	32	$0.883 \pm 0.027$	47	$0.597 \pm 0.022$
3	$2.069 \pm 0.033$	18	$1.209 \pm 0.027$	33	$0.824 \pm 0.025$	48	$0.611 \pm 0.022$
4	$1.764 \pm 0.031$	19	$1.289 \pm 0.028$	34	$0.830 \pm 0.024$	49	$0.604 \pm 0.023$
5	$1.794 \pm 0.031$	20	$1.236 \pm 0.028$	35	$0.820 \pm 0.024$	50	$0.473 \pm 0.021$
6	$1.752 \pm 0.031$	21	$1.257 \pm 0.028$	36	$0.783 \pm 0.024$	51	$0.443 \pm 0.020$
7	$1.716 \pm 0.031$	22	$1.313 \pm 0.029$	37	$0.758 \pm 0.023$	52	$0.418 \pm 0.019$
8	$1.804 \pm 0.032$	23	$1.085 \pm 0.029$	38	$0.802 \pm 0.024$	53	$0.398 \pm 0.019$
9	$1.528 \pm 0.031$	24	$1.042 \pm 0.027$	39	$0.815 \pm 0.025$	54	$0.440 \pm 0.020$
10	$1.484 \pm 0.029$	25	$1.041 \pm 0.026$	40	$0.867 \pm 0.026$	55	$0.433 \pm 0.020$
11	$1.499 \pm 0.030$	26	$1.041 \pm 0.026$	41	$0.626 \pm 0.024$	56	$0.458 \pm 0.021$
12	$1.511 \pm 0.030$	27	$1.000 \pm 0.026$	42	$0.600 \pm 0.022$	57	$0.283 \pm 0.018$
13	$1.481 \pm 0.029$	28	$1.033 \pm 0.026$	43	$0.641 \pm 0.022$	58	$0.331 \pm 0.019$
14	$1.504 \pm 0.030$	29	$1.021 \pm 0.026$	44	$0.622 \pm 0.022$	59	$0.268 \pm 0.018$
15	$1.512 \pm 0.030$	30	$1.049 \pm 0.027$	45	$0.572 \pm 0.021$		

TABLE VI. Acceptance corrected Dalitz plot distribution. The bin numbering is given in Fig. 4. The bin contents are normalized to the bin centered at  $X = 0, Y = 0$  (bin #27).

## ACKNOWLEDGMENTS

This work was supported in part by the EU Integrated Infrastructure Initiative HadronPhysics Project under contract number RII3-CT-2004-506078; by the European Commission under the 7th Framework Programme through the 'Research Infrastructures' action of the 'Capacities' Programme, Call: FP7-INFRASTRUCTURES-2008-1, Grant Agreement N. 227431; by the Polish National Science Centre through the Grants No. 86/2/N-DFG/07/2011/00320/B/H03/2011/40, 2011/01/B/ST2/00431, 2011/03/B/ST2/01847, 0312/B/H03/2011/40 and Foundation for Polish Science. We gratefully acknowledge the support given by the Swedish Research Council, the Knut and Alice Wallenberg Foundation, and the Forschungszentrum Jülich FFE Funding Program of the Jülich Center for Hadron Physics.

This work is based on the PhD thesis of Patrik Adlarson supported by Uddeholms Forskarstipendium.

- 
- [1] D. Sutherland, Phys.Lett. **23**, 384 (1966).
  - [2] R. Baur, J. Kambor, and D. Wyler, Nucl.Phys. **B460**, 127 (1996), arXiv:hep-ph/9510396 [hep-ph].
  - [3] C. Ditsche, B. Kubis, and U.-G. Meissner, Eur.Phys.J. **C60**, 83 (2009), arXiv:0812.0344 [hep-ph].
  - [4] H. Leutwyler, Phys.Lett. **B378**, 313 (1996), arXiv:hep-ph/9602366 [hep-ph].
  - [5] D. B. Kaplan and A. V. Manohar, Phys.Rev.Lett. **56**, 2004 (1986).
  - [6] D. Babusci *et al.* (KLOE-2 Collaboration), JHEP **1301**, 119 (2013), arXiv:1211.1845 [hep-ex].
  - [7] J. Bell and D. Sutherland, Nucl.Phys. **B4**, 315 (1968).
  - [8] J. A. Cronin, Phys.Rev. **161**, 1483 (1967).
  - [9] J. Gasser and H. Leutwyler, Nucl.Phys. **B250**, 539 (1985).
  - [10] J. Bijnens and K. Ghorbani, JHEP **0711**, 030 (2007), arXiv:0709.0230 [hep-ph].

- [11] J. Beringer *et al.* (Particle Data Group), Phys.Rev. **D86**, 010001 (2012), and 2013 partial update for the 2014 edition.
- [12] C. Roiesnel and T. N. Truong, Nucl.Phys. **B187**, 293 (1981).
- [13] A. Anisovich and H. Leutwyler, Phys.Lett. **B375**, 335 (1996), arXiv:hep-ph/9601237 [hep-ph].
- [14] J. Kambor, C. Wiesendanger, and D. Wyler, Nucl.Phys. **B465**, 215 (1996), arXiv:hep-ph/9509374 [hep-ph].
- [15] K. Kampf, M. Knecht, J. Novotny, and M. Zdrahal, Phys.Rev. **D84**, 114015 (2011), arXiv:1103.0982 [hep-ph].
- [16] S. Aoki *et al.*, “Review of lattice results concerning low energy particle physics,” (2013), arXiv:1310.8555 [hep-lat].
- [17] D. Alde *et al.* (Serpukhov-Brussels-Annecy(LAPP) Collaboration, Soviet-CERN Collaboration), Z.Phys. **C25**, 225 (1984).
- [18] A. Abele *et al.* (Crystal Barrel), Phys. Lett. **B417**, 193 (1998).
- [19] M. Achasov, K. Beloborodov, A. Berdyugin, A. Bogdanchikov, A. Bozhennok, *et al.*, JETP Lett. **73**, 451 (2001).
- [20] W. Tipples *et al.* (Crystal Ball Collaboration), Phys.Rev.Lett. **87**, 192001 (2001).
- [21] M. Bashkanov *et al.* (CELSIUS/WASA), Phys.Rev. **C76**, 048201 (2007), arXiv:0708.2014 [nucl-ex].
- [22] C. Adolph *et al.* (WASA-at-COSY Collaboration), Phys.Lett. **B677**, 24 (2009), arXiv:0811.2763 [nucl-ex].
- [23] S. Prakhov *et al.* (Crystal Ball at MAMI and A2 Collaborations), Phys.Rev. **C79**, 035204 (2009), arXiv:0812.1999 [hep-ex].
- [24] M. Unverzagt *et al.* (Crystal Ball at MAMI, TAPS and A2 Collaborations), Eur.Phys.J. **A39**, 169 (2009), arXiv:0812.3324 [hep-ex].
- [25] F. Ambrosino *et al.* (KLOE Collaboration), Phys.Lett. **B694**, 16 (2010), arXiv:1004.1319 [hep-ex].
- [26] F. Ambrosino *et al.* (KLOE Collaboration), JHEP **0805**, 006 (2008), arXiv:0801.2642 [hep-ex].
- [27] G. Colangelo, S. Lanz, and E. Passemar, PoS **CD09**, 047 (2009), arXiv:0910.0765 [hep-ph].
- [28] G. Colangelo, J. Gasser, B. Kubis, and A. Rusetsky, Phys.Lett. **B638**, 187 (2006), arXiv:hep-ph/0604084 [hep-ph].
- [29] C.-O. Gullstrom, A. Kupsc, and A. Rusetsky, Phys.Rev. **C79**, 028201 (2009), arXiv:0812.2371 [hep-ph].
- [30] S. P. Schneider, B. Kubis, and C. Ditsche, JHEP **1102**, 028 (2011), arXiv:1010.3946 [hep-ph].
- [31] B. Borasoy and R. Nissler, Eur.Phys.J. **A26**, 383 (2005), arXiv:hep-ph/0510384 [hep-ph].
- [32] J. Bijnens and J. Gasser, Phys.Scripta **T99**, 34 (2002), arXiv:hep-ph/0202242 [hep-ph].
- [33] M. Gormley *et al.*, Phys.Rev. **D2**, 501 (1970).
- [34] J. Layter *et al.*, Phys.Rev. **D7**, 2565 (1973).
- [35] A. Abele *et al.* (Crystal Barrel Collaboration), Phys.Lett. **B417**, 197 (1998).
- [36] C. Bargholtz *et al.* (CELSIUS/WASA), Nucl. Instrum. Meth. **A594**, 339 (2008), arXiv:0803.2657 [nucl-ex].
- [37] H. H. Adam *et al.* (WASA-at-COSY), “Proposal for the Wide Angle Shower Apparatus (WASA) at COSY-Juelich - ‘WASA at COSY’,” (2004), arXiv:nucl-ex/0411038.
- [38] R. Maier, Nucl.Instrum.Meth. **A390**, 1 (1997).
- [39] R. Bilger *et al.*, Phys.Rev. **C65**, 044608 (2002).
- [40] T. Rausmann *et al.* (ANKE Collaboration), Phys.Rev. **C80**, 017001 (2009), arXiv:0905.4595 [nucl-ex].
- [41] P. Adlarson *et al.* (WASA-at-COSY Collaboration), Phys.Lett. **B707**, 243 (2012), arXiv:1107.5277 [nucl-ex].
- [42] D. Babusci *et al.* (KLOE Collaboration), Phys.Lett. **B718**, 910 (2013), arXiv:1209.4611 [hep-ex].
- [43] R. Barlow, “Systematic errors: Facts and fictions,” (2002), arXiv:hep-ex/0207026 [hep-ex].